Understanding chemically processed solar cells based on quantum dots

Victor Malgras, Andrew Nattestad, Jung Ho Kim, Shi Xue Dou, Yusuke Yamauchi

Understanding chemically processed solar cells based on quantum dots

Victor Malgras[1], Andrew Nattestad[2], Jung Ho Kim[1,3],

Shi Xue Dou[3], and Yusuke Yamauchi[1,3]

1 *International Research Center for Materials Nanoarchitectonics (MANA), National Institute for Materials Science (NIMS), 1-1 Namiki, Tsukuba, Ibaraki 305-0044, Japan.*

2 *Intelligent Polymer Research Institute, University of Wollongong, Innovation Campus, North Wollongong, NSW 2500, Australia.*

3 *Institute for Superconducting and Electronic Materials, University of Wollongong, Innovation Campus, North Wollongong, NSW 2500, Australia.*

Photovoltaic energy conversion is one of the best alternatives to fossil fuel combustion. Petroleum resources are now close to depletion and their combustion is known to be responsible for the release of a considerable amount of greenhouse gases and carcinogenic airborne particles. Novel third-generation solar cells include a vast range of device designs and materials aiming to overcome the factors limiting the current technologies. Among them, quantum dot-based devices showed promising potential both as sensitizers and as colloidal nanoparticle films. A good example is the p-type PbS colloidal quantum dots (CQDs) forming a heterojunction with a n-type wide-band-gap semiconductor such as TiO_2 or ZnO. The confinement in these nanostructures is also expected to result in marginal mechanisms, such as the collection of hot carrier and generation of multiple exciton, which would increase the theoretical conversion efficiency limit. Ultimately, this technology could also lead to the assembly of a tandem-type cell with CQD films absorbing in different regions of the solar spectrum.

Keywords: solar cells; photovoltaics; quantum dots; lead sulfide; heterojunction

1. Historical aspects

A.E. Becquerel first observed the photovoltaic effect for the first time in 1839 by detecting small currents when silver chloride was illuminated [1]; but it was only in 1883 when C. Fritts deposited selenium on a thin layer of gold that the junction solar cell was first produced, albeit with an efficiency below 1%. The early 20th century is marked by significant advances in crystallography (P. Curie), solid state physics (J.J. Thomson, P. Drude, P. Debye, F. Bloch) and statistical physics (A. Einstein, M. Plank, L. Boltzmann), which provided the necessary knowledge to understand semiconductor-junction-based photovoltaic devices. Various architectures were attempted before D. Chapin developed a doped (diffused) silicon *p-n* junction based solar cell in Bell Laboratories in 1954 following R. Ohl's patent. The device, with an efficiency of around 6%, announced the first generation of commercially relevant solar cells. Most contemporary solar panels are still built on this crystalline silicon *p-n* junction technology attaining an efficiency of 26.3% (commercially available 21.5%) [2]. Combined with the invention of the transistor in 1947 (J. Bardeen, W. Shockley, and W. Brattain), which replaced *vacuum tube technology* by scalable electronics, the demand for manufactured semiconductors raised significantly. The price of silicon based solar cells dropped from USD 76.67/watt in 1977 to USD 0.60/watt in 2015, making the sun a competitive energy source, substituting for coal and other fossil fuels [3]. Nevertheless, researchers are still aiming to improve stability (life span, heat/moisture resistance), recyclability and especially conversion efficiency and fabrication costs.

For multiple reasons, researchers had to look in other directions, as this technology started to reveal certain limitations. W. Shockley and H. Queisser calculated in 1961 a theoretical limit specific to this type of single junction in *bulk* semiconductor solar cells restricting the efficiency to 33.7% (for 1 sun illumination) [4]. Moreover,

typical silicon purification lines require 650 °C baking processes [5] which are responsible for most of the energy cost of production. The National Renewable Energy Laboratory (NREL) keeps a detailed track of the certified efficiencies of various photovoltaic technologies which have appeared since 1975 (Figure 1). The 2nd generation of solar cells was aimed towards ecologically sustainable solutions and tried to decrease the amount of matter involved in the architecture of the device by using strongly light-absorbing materials such as 2-4 μm copper-indium-gallium-selenide (CIGS) thin films, which efficiently harvest most of the light in the 400-800 nm range. This technology can now achieve 21.7% conversion efficiency [7]. The 2nd generation also includes organic and dye-sensitized solar cells which are assembled through relatively simple and low-cost processes and able to reach efficiencies close to 12% [2]. The latter attracted considerable attention because of their *do it yourself* potential (simple technological manufacturing and low material purity requirements). These devices suffer from relatively short life-spans and instability, due to the use of molecular absorbers and liquid electrolytes, which make the devices hard to encapsulate. More recent research tends to address this drawback by using solid-state hole transporting materials [8], ionic liquids [9], or photonic crystal [10].

The 3rd generation solar cells target various strategies to overcome the Shockley-Queisser limit. The present record comes from tandem cells with 46% efficiency (using a concentrator), resulting from the stacking of several *p*-*n* junctions made from elements optimized to absorb specific regions of the solar spectrum. Unfortunately, such technology requires metalorganic vapour phase deposition techniques, which increase the cost of production by several orders of magnitude, thus making it only suitable for aerospace applications.

Another approach consists of using quantum dots (QDs) as light absorbers. Under a specific size, certain binary crystals show significant changes in their optoelectronic behaviour, making them an attractive option for photovoltaic technologies. The interest for quantum dot-based solar cells started when A. J. Nozik assumed in 2001 that marginal phenomena such as hot carrier collection and multiple exciton generation could significantly improve solar cell performances and thus, overcome the Shockley-Queisser limit [11,12]. Different methods exist to synthesize these nanocrystals, such as vapour-liquid-solid, molecular beam epitaxy, electron beam lithography, successive ionic layer adsorption and reaction, and the synthesis of colloidal quantum dots (CQDs) through nucleation processes.

The former three are *physical syntheses* and require highly controlled atmosphere, high voltage, and/or high vacuum, which hinder their widespread application. The other methods, known as *chemical syntheses*, are relatively cheap to set up, but require significant optimization in order to obtain controlled size and size distribution. Moreover, one has to replace the long organic ligand used for the synthesis process, capping the colloidal QDs to prevent agglomeration, by smaller molecules. There is a great deal of research which is currently aiming to improve this *ligand exchange* method and thus improve the performance and stability of the device. There are three main designs that have been investigated to achieve proper photovoltaic devices: the Schottky junction, the quantum dot sensitizer and the depleted heterojunction. The last architecture has recently achieved 10.7% efficiency through the use of hybrid passivation methods [13]. This review presents a brief survey of the typical principles of operation of solar cells and narrows down to place colloidal quantum dot-based device in their technological context.

2. Operation of solar cells

Solar cells can be seen as diodes in which the generation current can be greatly increased due to the ability of the material to absorb photons, thus exciting electrons which will contribute to the typical thermally generated current.

2.1. Solar spectrum and solar simulator

Many factors can affect spectral irradiance distribution, such as the latitude, time of the year, and time of the day, as well as with the weather conditions, (clouds, humidity, wind, *etc.*). In order to define a *standard sun* used to compare the efficiency of photovoltaic devices, one can refer to the air-mass (AM) index that relates to different conditions. AM 0 corresponds to the solar spectrum above the edge of the atmosphere and AM 1.0, 1.5, and 2.0 express the solar irradiance from the sun after passing through the atmosphere with angles of 0, 48.2 and 60.1°, respectively (see Figure 2). This gaseous mass is composed of various compounds which absorb a significant proportion of the light intensity (up to 23%). AM 0 is therefore only suitable for extraterrestrial applications (e.g. satellites) while the others provide insight on the input power a solar cell can absorb in a day. AM 1.0 is exact only for devices installed in equatorial or tropical regions at the zenith. Most of the Earth's population living further from the equator in temperate zones where the light path across the atmosphere is longer, AM 1.5 represent a much more relevant standard. Some other factors include the *albedo* of the surroundings (diffuse reflectivity of a surface). For these reasons, most solar simulators use a xenon arc lamp with appropriate filters mimicking the AM 1.5 spectrum.

2.2 p-n junction under illumination and the Shockley-Queisser limit

Under dark conditions, the generated current comes from thermally activated charge

carriers. Photons conveying more energy than phonons (lattice vibrations, E_{ph} < 100 meV), their contribution to the generation current can quickly become significant. Indeed, most of the solar spectrum is spread between 250 nm (4.96 eV) and 4000 nm (0.31 eV), divided between ultraviolet (UV), visible, and infrared (IR) light.

As described by Shockley and Queisser in 1961 [4], the mechanisms responsible for conversion and extraction limit the efficiency of standard solar cell to 33.7%. First, photons with energy lower than the forbidden bandgap of the material (E_G) will be diffracted, reflected, or transmitted through the junction. This phenomenon is accountable for the loss of 19% of the solar energy in a typical standard crystalline silicon solar cell with $E_G \approx 1.1\ eV$ (see Figure 3). Secondly, in the case where a photon transfers an energy $E_{h\nu}$ higher than E_G to an electron, the latter will be excited to a higher energy level to further thermalize to the bottom of the conduction band (E_{CB}) by releasing a phonon with an energy $E_{ph,e}$ (analogously $E_{ph,h}$ for holes) with $E_{ph,e} + E_{ph,h} = E_{h\nu} - E_G$. This other mechanism is responsible for 33% solar power loss. Finally, phenomena such as the radiation of the photovoltaic device (black body radiation) and radiative recombination (detailed balance principle) also account for another ~15% loss of the incoming solar energy.

In a solar cell under *short circuit conditions* (Figure 4(a)), the diffusion flow remains unchanged, but most of the photogenerated charges drift along the electric field. The short-circuit current density, J_{sc}, is maximum and corresponds to the photogenerated charges diffusing towards the depletion region to be driven along by the junction polarity V_{bi} (the built-in potential). The main limitation resides in properties such as the diffusion length and the minority carriers' lifetime, which can bring them to recombine before reaching the electric field. If a load resistance is added to the circuit,

however, charge extraction is restricted. Once the collection rate decreases below the photogeneration rate, excess minority carriers accumulate on each side of the depletion region, gradually splitting the quasi-Fermi levels associated to the valence and conduction bands (E_{FV} and E_{FC}, respectively) and building up a polarity opposed to the applied potential drop. This causes the diffusion current to increase. The recombination probability (or recombination rate) depends strongly on the number of excess carriers, until equilibrium conditions are reached to satisfy:

$$J_{ph} - J_{rec} - J = 0 \qquad (1)$$

with J_{rec} being the overall recombination current density, $J_{ph}$the photogenerated current density and J the current density exiting the cell. Any photogenerated charges which cannot be extracted will thus necessarily recombine.

Under *open circuit conditions* (infinite load resistance), excess charges are confined in the device, and equilibrium is reached when the generation and recombination rates are equal (Figure 4(b)). Under these conditions, each side of the depletion region hosts its maximum possible carrier density, and the quasi-Fermi levels are separated by an energy qV_{oc}, where V_{oc} represents the maximum electrical potential which can be achieved in the device.

Any intermediate states of the charge flow can theoretically be derived from Shockley ideal diode approximation:

$$J = J_{ph} - J_0\left(e^{\frac{qV}{kT}} - 1\right) \qquad (2)$$

This typical current density-voltage relation is the principal figure of merit to assess the performance of a solar cell and is further discussed in the following section.

2.3 Solar cells characteristics: ideal vs. real

The principal information regarding the performance of a solar cell resides in the current density – voltage ($J-V$) characteristic. The short-circuit current density (J_{sc}) is the maximum current that can be collected from the device and reflects the output of a broad set of properties such as photo-absorption, injection/diffusion, junction engineering, and defect/impurity levels. In general, J_{sc} will depend on:

- the ability of the active material to strongly absorb light;
- how fast is the injection from the absorbing material to the transport material compared to the back-surface recombination process;
- the potential distribution through the cell containing the least barriers/well which could act as recombination centres.

For optimally engineered solar cells, the short-circuit current density can be expressed as:

$$J_{sc} = qG(D_N + W + D_P) \qquad (3)$$

where G, W, D_N and D_P are the charge generation rate (includes absorption spectrum and injection rate), the depletion region's width, and the diffusion lengths of minority carriers (electrons and holes), respectively.

Figure 5 shows a typical $J-V$ curve and highlights the most relevant parameters. The maximum power, P_{max} with coordinates (V_{mp},J_{mp}), which can be obtained by plotting the power curve $P = V \times J$, determines under which regime the solar cell should operate in order to optimize its output. From this value, one can calculate the *fill factor* (FF):

$$FF = \frac{V_{mp} \times J_{mp}}{V_{oc} \times J_{sc}} = \frac{P_{max}}{V_{oc} \times J_{sc}} \quad (4)$$

provides insight on the *squareness* of the solar cell response is. Higher fill factors are attributed to more ideal devices: they result in higher and more stable power as the input conditions fluctuate. Finally, the device efficiency represents the ratio between the maximum power output and the power input:

$$\eta(\%) = 100 \times \frac{P_{max}}{P_{in}} \quad (5)$$

with $P_{in} = 100\ mW/cm^2$ for the 1.5 AM standard.

3. Quantum dots: properties and synthesis

Quantum dots are small particles (or nanocrystals) with electronic properties which differ from those of their bulk counterpart due to their reduced size. This section compiles their properties of interest in the context of solar cells, the different methods of synthesis, and their role in different photovoltaic device architectures.

3.1. Confinement in quantum dots

The so-called *particle-in-a-box* model is the most comprehensive example to introduce confinement in quantum mechanics, describing how the energetic configuration of a particle depends on the size and shape of the space it is confined in. The energy levels available for a particle of mass m, confined in a box of size L, can be obtained by solving the Schrödinger equation for the single dimension case with infinite potential boundaries [14]:

$$E_n(k_n) = \frac{\hbar^2 k_n^2}{2m} = \frac{n^2 \hbar^2 \pi^2}{2mL^2} \quad (6)$$

where $\hbar$, k_n and n are respectively the reduced Planck constant, the wavenumber and an

integer justifying mathematically the terms *discrete* (or *quantized*) energy levels. The energy between E_n and E_{n+1} increases as the size of the box L decreases and becomes negligible at macroscopic levels.

QDs are semiconducting nanocrystals that are small enough to be considered as potential wells (similar to the particle-in-a-box) within which electrons undergo confinement regime. This regime is considered to be *strong* when the size of this three-dimensional box becomes smaller than the theoretical distance between embedded electron and hole, the exciton Bohr radius a_{exc}:

$$a_{exc} = \frac{a_0 \varepsilon_r}{m^*/m_0} \qquad (7)$$

with $a_0 = 0.529\text{Å}$, ε_r, $m^* = \left(\frac{1}{m_e} + \frac{1}{m_h}\right)^{-1}$, and m_0 being the hydrogen atom's Bohr radius, the relative permittivity constant of the material, the electron-hole reduced mass, and the free electron mass, respectively. For example, in the case of lead sulfide with $m_e = m_h = 0.08 m_0$ and $\varepsilon_r = 17.2$, we obtain $a_{exc} = 21.4\, nm$. This value is a first approximation, as it does not take into consideration effects due to the dielectric properties of the crystal. Other factors, will also be responsible for modifying the boundary potential seen by the confined charge in a nanocrystal and thus, affecting the energy states distribution, such as shape symmetries (or asymmetries), surface reconstruction and additional chemical interactions.

3.2. Tunable bandgap

In the quantum confinement regime, variations in band edge energy level positions will become significant. Louis E. Brus [15] first reported the effective mass model to evaluate the bandgap of QDs:

$$E_{G,QD} = E_{G,Bulk} + \frac{\hbar^2 \pi^2}{2 m^* R^2} - \frac{1.8 q^2}{\varepsilon_{QD} R} + polarization\ terms \qquad (8)$$

where R and ε_{QD} are the radius and the dielectric constant of the QD, respectively. Lead chalcogenides, however, have relatively high dielectric constants and small bandgaps (see Table 1). The model deviates from real experimental data for crystal sizes under 10 nm (see Figure 6) as the common approximations employed to solve the Schrödinger equation do not hold anymore. Wang *et al.* developed a hyperbolic model [16] overcoming this discrepancy and rewrote the equation as:

$$E_{G,QD} = \sqrt{E_{G,Bulk}^2 + \frac{2h^2 E_{G,Bulk}}{m^* R^2}} \qquad (9)$$

Another method was later proposed, using a complex 4-band model [17,18] using the $\boldsymbol{k} \cdot \boldsymbol{p}$ Hamiltonian:

$$E_{Vac,QD} = E_{\boldsymbol{k}\cdot\boldsymbol{p}} + \left(1 - \frac{1}{\varepsilon_{QD}}\right)\frac{q^2}{2R} + \chi_{bulk} \qquad (10)$$

where $E_{Vac,QD}$ is the energy level relative to vacuum, $E_{k\cdot p}$ is the energy level from the $\boldsymbol{k} \cdot \boldsymbol{p}$ calculation, and χ_{bulk} is the electron affinity of the bulk.

When it comes to band structure engineering of electronic devices and specifically designing the desired properties of homo- or heterojunctions, tuning the bandgap has significant advantages. For example, many photovoltaic devices require the use of type II semiconductor junctions (staggered gap) for effective charge injection, transport, and collection.

3.3. Electron-hole pairs, excitons

In bulk junction semiconductor devices, *electron-hole pairs* are formed by considering the final state of an excited electron as being *in* the conduction band, leaving a hole behind in the valence band and having both charges swept away from each other by the electric field in the depleted region. In reality, however, this only hold for macroscopic

materials where the long-range periodicity of the lattice ensures that the electronic properties remain locally the same, wherever the charges are located. In nanostructured devices, many new parameters must be taken into account: crystal boundaries, shape effect, and interface tunnelling. They can be seen as defects introducing perturbations which result in potential wells, barriers and mid-gap states.

For example, in crystals with high dielectric constants, the Coulomb interactions between electrons and holes can be screened. Therefore, they become weakly bound and form a quasi-particle called an *exciton*. Its energy state can be calculated by solving the Schrödinger equation for the hydrogen atom, replacing the mass of the proton by the effective mass of the hole from the material considered. In bulk materials, the excitonic levels are located in the bandgap near the conduction band (see Figure 7), reflecting the Coulomb interaction. Excitons have no net charge, but can travel in a medium until they receive enough energy to split. In bulk materials, this can be as low as the thermal vibrations at room temperature ($\Delta E \approx k_B T$). In isolated quantum dots (such as PbS quantum dots), it is well established that there is no *free charge* state, because ~~since~~ the excited electrons and holes are spatially confined, therefore and the whole transitional spectrum is entirely dictated by excitonic levels [19-23].

3.4. Relaxation dynamics, hot carriers, and multiple exciton generation

When an electron absorbs a photon with an energy which is above the energy of the lowest exciton energy (generally referred as $1S_h$-$1S_e$), various pathways can occur:

(1) the electron may thermalize to its lowest state by dissipating energy as lattice vibration through electron-phonon interaction or Auger process;

(2) the excess energy can be transferred to one or more electrons through reverse Auger process, resulting to multiple exciton generation (MEG);

(3) the electron-hole quasi-particle can split, leaving a highly energetic charge (hot carrier) that must be extracted rapidly before recombining.

Pathway (1) results in an obvious energy loss (Shockley-Queisser limit) and is still the most probably fate of excited charges because of its extremely fast occurrence in bulk semiconductors (~ ps). Theoretical models have shown that these processes can be slowed down when the photogenerated carrier density is increased up to ~10^{18} cm^{-3}, thus inducing a *hot phonon bottleneck* due the non-equilibrium distribution of longitudinal optical (LO) phonons (pathways (2) and (3)) [24,25]. Later on, Nozik and co-workers showcased the potential of this effect if applied in optoelectronic devices [26-28]. This process is, however, still limited by crystal momentum which must be conserved during the transitions. Therefore, MEG was only be observed in bulk semiconductors for $h\nu > 4E_G$ [29]. For QD-based devices, however, research groups report more and more promising results demonstrating enhanced photoconversion efficiencies through MEG, even under AM 1.5 conditions [30-32].

Because of their small size, QDs do not suffer from the limitations related to conservation of momentum which is generally inherent to long-range periodicity (Figure 8). These assumptions arise from the idea that if the energy separation between two discrete exciton levels is higher than the fundamental phonon energy, multiple-phonon processes would be necessary in order for the charge to relax to the lowest level. These mechanisms are significantly slower than single phonon interactions, and their relaxation time could then be estimated from:

$$\tau_c \approx \omega^{-1} exp(\Delta E / k_B T) \qquad (11)$$

where τ_c is the hot carrier cooling time, ω is the phonon frequency and ΔE is the energy level separation. According to Equation (11), strongly quantized levels (> 0.2 eV)

would extend the relaxation time to ~100 ps. Using ultra-fast transient absorption spectroscopy or time-resolved photoluminescence decay [33-35], Schaller *et al.* observed different decaying components, which were associated to single- and multiple-excitons.

These properties , if fully exploited in solar cells technology [12,29], are expected to enhance the Shockley-Queisser limit (Figure 9) from 33.7% to 45% (for MEG) [36] and to 67% (for hot carriers collection) [37]. Until now, however, these measurements were only successfully performed on individual nanocrystals under controlled conditions. The challenge of incorporating QDs into a photovoltaic device while taking advantage from MEG [38-41] or hot carrier [42,43] mechanisms is still attracting a lot of attention.

3.5. Synthesis

Different methods have been investigated to produce QDs of different materials, with various shapes, sizes and size distributions for a multitude of applications. Physical-chemical vapour deposition techniques generally involve the growth/formation of the materials directly on a substrate, giving an improved control over the size and spatial distribution. They are especially appropriate for the fabrication of superlattices which amplify quantum electronic confinement properties [44-46]. On the other hand, wet chemical techniques provide good alternative routes to producing QDs in a colloidal suspension (CQDs) with 3D quantum confinement characteristic. These methods typically use standard glassware with temperatures below 300 ºC, significantly reducing the production costs.

3.5.1 Physical vapour deposition

A standard method to grow a 3D structure through vapour phase deposition is the

Stranski-Krastanov growth [47-49]. By depositing several monolayers of semiconductors with a strong lattice mismatch, epitaxial growth can be initiated in a layer-by-layer fashion and to coherently grow ~~forms~~ 3D islands (Figures 10(a)-(f)) [50].

Another widely reported technique is the vapour-liquid-solid (VLS) deposition [51-55], where a thin film of gold (1-10 nm) is typically deposited onto a silicon wafer (100) and heated above the Au/Si eutectic point to form droplets of Au-Si alloy on the surface of the substrate. The sample is then placed inside a vacuum chamber with a flow of reactive gas mixture (typically $SiCl_4$:H_2) at 800 ºC. The gas is absorbed into the droplets, which act as a catalyst to lower the activation energy of normal vapour solid growth, until supersaturation is reached. This is followed by the excess Si atoms to be automatically driven down to the substrate, leading to anisotropic growth (see Figures 10(g)-(i)).

3.5.2 Successive ionic layer adsorption and reaction (SILAR)

Vogel *et al.* reported the sensitization of wide-band-gap semiconductors with various binary sulfides semiconductor nanoparticles through chemical bath deposition [56]. The method was further renamed later on as SILAR in order to prevent the confusion with other types of chemical bath deposition techniques. The technique consists in the successive immersion of the substrate in aqueous solution of salts (*e.g.*, lead nitrate followed by sodium sulfide). The deposition can be controlled by varying the immersion time, the number of repetitions, the type of salt or the concentration. The number of *seeds* deposited during the first cycle remains a limiting factor, however, as any subsequent steps will only *feed* the pre-existing crystallites. The direct growth on the substrate has the advantages of increasing the cohesion of the sensitizer and thus improving electron injection. This method, which, for instance, is used for the fabrication of quantum dot sensitized solar cells, suffers still from certain drawbacks

which will be discussed in section 4.1.1 [57].

3.5.3. Colloidal growth synthesis

After Faraday synthesized gold colloidal nanoparticles in 1857 [58], many other chemical routes were developed in order to obtain similar nanostructures with a wide range of binary compositions. A typical method involves the combination of two (or more) precursors, generally from groups II/VI or IV/VI, in a hot solvent containing carefully selected coordinating molecules under vigorous stirring. At the start, a multitude ~~A~~ of nucleation centres are formed, initiating the growth of particles through Ostwald ripening. The role of the coordinating ligands is to set a critical crystal size, after which, the sterically hindered growth leads to a narrowed size distribution [59-61]. The mean size can be empirically controlled through parameters such as the precursor ratio, ligand concentration, temperature and reaction time. These techniques developed and modernized by Murray *et al.* in IBM's laboratory remain, even nowadays, the standard recipes for the synthesis of cadmium and lead chalcogenides [62-64]. Typically, tri-n-octylphosphine (TOP) is used to dissolve the chalcogen (S, Se, Te) precursor, and tri-n-octylphosphine oxide (TOPO) act as the coordinating ligand (Figure 11(a)) [65]. They also introduced the combination of lead oleate-bis(trimethylsilyl)sulfide precursor to produce PbS quantum dots in hot diphenyl ether (boiling point ~260 ºC). Nowadays, researchers are generally adopting the Hines and Scholes method [66], in which toxic diphenyl ether is replaced by 1-octadecene (boiling point 315 ºC). The synthesis must be followed by appropriate washing to extract the quantum dots from the reaction solution and remove unreacted ligands and precursors. The final product remains capped with oleate (or TOPO) molecules, making it stable in non-polar solvents, hence the name *colloidal* quantum dots. Parameters such as injection temperature and reaction time can be accurately controlled to produce a wide

range of nanoparticle sizes, and thus a wide range of bandgaps with different absorption cut-off and emission wavelengths (Figure 11(b)).

4. Quantum dots for photovoltaic application

QDs show unique optoelectronic properties due to their extreme confinement, including a high extinction coefficient allowing thin layers to absorb a significant portion of incident photons. There has been considerable research aiming to design devices with the purpose of optimizing photo-absorption and charge transport/collection while maintaining a high voltage output. Researchers use various architectures as scaffolds to observe the effects of new materials and new treatments, and to study the fundamentals of electronic transport.

4.1. Typical device architectures

Here, three different architectures are reviewed (Figure 12): the quantum dot sensitized solar cell, the colloidal quantum dot Schottky junction solar cell and the colloidal quantum dot heterojunction solar cell [68,69]. Other strategies, not covered in the current review, have more recently been investigated, such as hybrid cells blending colloidal quantum dots with polymers [70-73], fullerenes [74,75], graphene [76,77], or carbon nanotubes [78].

4.1.1. Quantum dot sensitized solar cell (QDSC)

Inspired by their organic counterparts (dye-sensitized solar cells, DSCs), the inorganic sensitizers from QDSCs are generally grown through SILAR deposition and are selected for being strongly light-absorbing in the visible range. The operation mechanism can be briefly summarized as: i) a photon is absorbed in a QD, generating an exciton; ii) the electron and hole dissociate at the interface with a TiO_2 particle; iii)

the electron is injected into the TiO_2, resulting in the oxidation of the QD sensitizer, and iv) is transported to the working electrode, which is typically a transparent conductive oxide (TCO); v) the hole recombines with an electron from a redox medium and regenerates the ground state; vi) Finally the system is at equilibrium once the oxidized electrolyte diffuses to the counter electrode where it is reduced.

Typical electrolytes in DSCs use the iodide/triiodide redox couple; it is however a reactive source of corrosion for the QD sensitizers. Other compositions, including polysulfides dissolved in methanol [79], cobalt complexes [80] or solid state hole conductors such as (2,2(,7,7(-tetrakis-(N,N-di-pmethoxyphenylamine) 9,9(-spirobifluorene) (spiro-OMeTAD) [81], have shown more stable performance. As in DSCs, the main detrimental pathway for photogenerated carriers to recombine in QDSCs is from the TiO_2 conduction band into the redox couple from the electrolyte [82,83]. This can be explained from the low coverage efficiency during the SILAR deposition. Generally, a ZnS coating efficiently screens these back-recombination mechanisms, but it can also introduce new monoenergetic surface states affecting the fill factor [84]. Various other strategies are still being investigated [85-89]. The latest devices sensitized with PbS quantum dots showed short-circuit current as high as 20.8 mA/cm^2, leading to an overall efficiency of 8.2% [90].

4.1.2. CQD Schottky junction solar cell (SJSC)

The CQD SJSC was the first of its kind to achieve efficiencies beyond 1% from CQDs [91]. The architecture is based on overlaying a TCO with large work function (such as indium-doped tin oxide) with a film of *p*-type CQDs to form an Ohmic contact. This is followed by evaporating a metal with a shallow work function (aluminium, magnesium) to generate an appropriate band-bending suitable to extract electron while screening holes.

This attractive strategy had, however, a few limitations. The short diffusion length in these films limits their thickness to 200 nm, which is too thin to absorb a sufficient portion of the incident radiation. Increasing the thickness of the device above this critical limit causes charge recombination to become a substantial problem. Also, the Fermi level can be easily pinned by defect states at the metal/semiconductor interface, affecting the overall open-circuit voltage. Nevertheless, optimization of the material synthesis, post-treatments, and assembly [92], along with carefully engineered hole-selective contacts, allowed Piliego *et al.* to produce devices with an efficiency of 5.2% [93].

4.1.3. CQD depleted heterojunction solar cell (DHJSC)

This architecture has similar aspects to the CQD SJSC, except that it has an additional *n*-type layer of wide-band-gap semiconductor particles (TiO_2, ZnO) between the TCO electrode and the CQD layer to secure electron transport. The back contact is typically made of a metal with a large work function (such as Au or Pt).

As compared to the SJSC, the mild depletion region of heterojunction provides more efficient electron-hole dissociation, and because it is located on the illuminated side, carrier separation happens faster. Back electron transfers from the oxide to the CQD layer can be effectively suppressed by the built-in field. Finally, a higher open-circuit voltage can be achieved because of the large difference between the Fermi level of the TiO_2 and the work function of the counter electrode. The first DHJSC [69] was reported in 2010 with an efficiency of 5.1%, far beyond the records previously achieved by other architectures at the time. This high performance was partly due to optimized parameters such as: CQD synthesis, size selection, ligand exchange and film thickness (both for TiO_2 and PbS CQDs). Further improvement, including controlled oxide doping and inorganic passivation, enhanced the performance of these solar cells up to

7.4% [94-97]. Ultimately, strategies such as replacing the wide-band-gap oxide by n-doped CQD film and stacking films with different QD size were considered to fabricate promising tandem structures to increase the absorption range [98-101].

4.2. The role of the ligands

Ligands are ions or molecules coordinating with a metal atom [102]. In the context of nanocrystal chemistry, ligands form a bond with surface atoms where, by definition, the periodicity is interrupted and fulfils three main roles: passivation, functionalization, and steric spacing.

The term *passivation* literally implies that a material is made less reactive to its environment. The surface of nanoparticles can be unstable due to strains, uncontrolled reconstruction, or unbalanced charge. These reactive sites are ready to bond with any adventitious moieties so as to lower its surface energy. The most common contaminants are the oxides formed from oxygen and moisture in air. These species generally have a detrimental impact on the particle properties by adding new localized surface states (generally mid-gap states) to the overall crystal energy structure. These levels can not only pin the Fermi level down (and thus lower the open-circuit voltage), but also act as deep traps and recombination centers. Surface passivation usually involves the introduction of ligand molecules (or ions) to coordinate with these unstable sites. An efficient passivation will induce a minimum change in the energy state distribution, while preventing other adventitious contaminants from being adsorbed.

The term *functionalization* has a broad meaning, as it includes any modification in the physical or chemical reactivity of the material. For instance, in the context of biotechnology, CQDs can be functionalized to improve their biocompatibility [103] or can act as a fluorescent chromophore binding to specific cells or proteins [104]. For PbS CQD-based solar cells, the nanoparticles are coated with oleate ligands having long

non-polar hydrocarbon chains. This has the effect to neutralize the apparent surface charge, thus giving the material the ability to be suspended in non-polar solvents (e.g., alkanes, toluene, chloroform). This enable the ability of CQDs to be deposited on substrates through spin-coating, dip-coating or even potential screen- and inkjet-printing techniques [105].

In order for QDs to retain their confined optoelectronic properties, they must maintain a certain degree of isolation, thus preventing the electron wave function from delocalising in neighbouring nanocrystals. The loss of confinement leads to uncontrolled and non-uniform energy level reconfiguration; the first exciton transition is reduced and the electronic landscape regains its continuous character (from the bulk). On the other hand, electrons from completely remote nanoparticleshave a very low hopping probability and thus suffer from low conductivity. After being cast on a solid surface, ligands of different lengths provide various *steric spacing* between the QDs and a balance must be found between quantum confinement and electronic conductivity. For this reason, CQD films are generally made through a layer-by-layer process, where ~~in~~ each cycle consists in exchanging long chain ligands for shorter ones (see Figures 13(a) and (b)). Ligand exchange can roughly be categorized into two groups: organic and inorganic.

4.2.1. Organic ligand exchange

Replacing oleate molecules with short ionic dithiol ligands such as 1,2-ethanedithiol (EDT) and 1,3-benzenedithiol (BDT) is a promising strategy to improve connectivity in PbS CQD films [106-111]. Some groups, however, have reported poor resistance to ambient atmospheric conditions [112,113]. Later on, optimized ligand exchanged employing 3-mercaptopropionic acid (MPA) seemed to lead to better stability, improved mobility, and the resulting film was less influenced by possible trap states for

similar interparticle spacing (Figures 13(c) and (d)) [114]. Jeong *et al.* suggested that the greater chemical diversity of MPA (thiol + carboxylic groups) in comparison to EDT can be responsible for passivating a broader distribution of surface states [115]. Through modelling and X-ray photoelectron spectroscopy analysis, it was found however that the ligand coverage efficiency, and thus the stability of the particle surface, could be hindered by hydroxylation mechanisms [116,117]. It was also reported that substituting the oleate group for oleylamine [118] or octylamine [119] through a 3-day solution-phase ligand exchange prior to the MPA or EDT solid phase exchange promoted a more effective replacement and improved passivation. More recently, Giansante *et al.* reported a complete study of PbS CQDs passivated with various types of short conjugated ligands and were able to enhance their broadband light absorption while maintaining their stability [120].

4.2.2 Inorganic ligand exchange

Because of their bulkiness as well as their vulnerability to thermal degradation and oxidation, other researchers have aimed to substitute organic ligands for their inorganic analogues. Talapin's group started by using $Sn_2S_6^{4-}$ ions to cap various types of quantum dots (CdSe, CdTe, CdS, Bi_2S_3, Au, Pd) and extended this work further with a wider range of inorganic ligands such as HS^-, Se^{2-}, HSe^-, Te^{2-}, HTe^-, TeS_3^{2-}, OH^-, NH^{2-} and S^{2-} (Figure 14(a)) [121-123]. In a similar vein, Yang *et al.* tuned the external quantum efficiency by supressing Auger recombination through adjusting the composition of the outer and intermediate shells of core-shells structure [124]. Supran *et al.* also improved shortwave-infrared device performance by engineering PbS-CdS core-shell CQD in a type IV LED (organic-CQD-inorganic structure) [125]. Other promising methods include atomic chlorine ligand passivation (Figure 14(b)), leading to improved electronic transport [126,127]. After completely removing the oleate ligand

using ammonium sulphide, Zhang *et al.* reported that the remaining QDs were self-passivated and interconnected through metal-sulfide bonding [128]. Cate *et al.* observed the activation of carrier multiplication after infilling PbSe films with Al_2O_3 or Al_2O_3/ZnO by atomic layer deposition using microwave conductivity transients [129]. Kinder *et al.* assembled various solar cells that could reach an efficiency of 2.4% from a matrix of PbS QDs encapsulated in a CdS matrix, creating a quasi-superlattice [130].

In their inorganic halide ligand passivation method, Tang *et al.* successfully improved passivation due to surface sulfur dangling bonds by treating the quantum dots in a mixture of tetradecylphosphonic acid, $CdCl_2$, and oleylamine (60 ºC, 5 min) (Figure 14(c)) [96]. This improved the stability and size distribution by removing certain surface defects. The spin-coating process took place in a glove box where each sub-layer was then post-treated with solutions of cetyltrimethylammonium bromide (Br^-), hexadecyltrimethylammonium chloride (Cl^-), or tetrabutylammonium iodide (I^-). These treatments improved the device performance significantly [131,132]. Thon *et al.* also studied the evolution of mid-gap trap-states after such a passivation by *ab initio* calculations [133]. Ip *et al.* performed further optimization, leading to a solar cell with 7.4% efficiency [97].

4.2.3. Transport in CQD depleted heterojunction solar cells

Recently, the term *selective contact* has been considered as a better description for the role of these collecting junctions, compared to *heterojunctions*. Mora-Sero *et al.* clearly observed how the choice of material can literally screen the charges: fluorine doped tin oxide, Au or poly(3,4-ethylenedioxythiophene) (PEDOT) for holes; TiO_2 or ZnO for electrons [134]. It was also reported that major back surface recombination mechanisms can be suppressed by simply adding hole [135] or electron [136] selective contacts. The appropriate selection of materials and doping techniques have been at the center of

considerable attention when it comes to engineering the interface between PbS CQDs and the electron selective contact [137-141]. Hole collection was successfully improved by using LiF in Schottky devices [142-145], while DHJSC shows better results using MoO_X (see Figure 15(a)) [146,147]. Gao *et al.* also reported that hole injection could be controlled through Schottky barrier engineering [148]. This could be achieved by align the work function of the metal with the energy bands of the PbS CQDs with specific sizes.

Bakulin *et al.* observed that charge immobilization and poor charge separation were caused by the presence of trap states with various depths (0.3-0.5 eV) below the conduction band (see Figure 15(b)) [149]. Using 1D and 3D models and taking into consideration the geometry of the device and its photoluminescence response, Zhitomirsky calculated the lifetime, trap density, mobility, and diffusion coefficient [150]. He found that state-of-the-art devices have an effective diffusion length of 80 nm. Recently, Whitham *et al.* demonstrated that charge localization can be greatly suppressed by reducing the level of disorder in CQD films, by epitaxially connecting ordered PbSe nanocrystals [151].

Surface passivation can have a considerable impact on transport in CQD films which is substantially mediated by intraband (in-gap) states [152]. Using an optical field-effect transistor configuration, Nagpal and Klimov described the existence of a *mid-gap band* with different levels of participation to charge transport, depending on whether the device is in the dark or under illumination (Figures 15(c)-(e)) [153]. Using similar methods, Stadler *et al.* employed sub-threshold analysis to determine the trap distribution and map the density of state distribution in CQD films [154].

5. Concluding remarks and outlook

A tremendous effort has been deployed to analyse and exploit the properties of

nanostructures such as quantum dots in order to assess their applicability in the field of photovoltaic and other optoelectronic devices. While theoretical speculations and calculations place these materials at the centre of the third-generation solar cells, recent research output tends to demonstrate that many unpredictable issues arise from the implementation of such structures inside devices. The considerable work targeting material synthesis and device engineering, however, is gradually circumventing these hindrances, opening the door to a potential solar cell technology which could be entirely fabricated through chemical processes and thus, at lesser costs. For example, recent attempts have been aiming to hybridize PbS quantum dots with methylammonium lead halide perovskite, and achieved an unprecedented efficiency of 10.6% [155-157]. Nowadays, extensive research aims at nanostructuring a wide range of materials [158-160], including the promising lead halide perovskite [161-164], to further improve the efficiencies and versatility of nanocrystal-based optoelectronic devices.

Acknowledgements

V.M. is an overseas researcher under Postdoctoral Fellowship of the Japan Society for the Promotion of Science (JSPS). A.N. would like to thank the Australian Renewable Energy Network (ARENA, project 6-F020) and the Australian Research Council (DE160100504) for funding as well as the ARC Centre of Excellence for Electromaterials (ACES) for support in the preparation of this manuscript.

References:

[1] Becquerel AE. Mémoire sur les effets électrique produits sous l'influence des rayons solaires [Essay on electric effects occuring under the influence of solar radiation]. C R Hebd Seances Acad Sci. 1839;9:561-567.

[2] Green MA, Emery K, Hishikawa Y, *et al.* Solar cell efficiency table (version 49). Prog Photovolt: Res Appl. 2017;25(1):3-13.

[3] Transparent Cost Database - OpenEI [Internet]. Golden (CO): National Renewable Energy Laboratory. 2009-2015 [cited 2017 Jan 6]. Available from: http://en.openei.org/apps/TCDB.

[4] Shockley W, Queisser HJ. Detailed balance limit of efficiency of p-n junction solar cells. J Appl Phys. 1961;32(3):510-519.

[5] Becker C, Ruske F, Sontheimer T, *et al.* Microstructure and photovoltaic performance of polycrystalline silicon thin films on temperature-stable ZnO:Al layers. J Appl Phys. 2009;106(8):084506.

[6] NREL Photovoltaic Research [Internet]. Golden (CO):NREL;2016 (cited on 2017 Jan 5). Available from http://www.nrel.gov/pv

[7] Jackson P, Hariskos D, Wuerz R, *et al.* Properties of Cu(In,Ga)Se_2 solar cells with new record efficiencies up to 21.7%. Phys Status Solidi RRL. 2015;9(1):28-31.

[8] Bach U, Lupo D, Comte P, *et al.* Solid-state dye-sensitized mesoporous TiO_2 solar cells with high photon-to-electron conversion efficiencies. Nature. 1998;395(6702):583-585.

[9] Kuang D, Comte P, Zakeeruddin SM, *et al.* Stable dye-sensitized solar cells based on organic chromophores and ionic liquid electrolyte. Solar energy. 2011;85(6):1189-1194.

[10] Chung I, Lee B, He J, *et al.* All-solid-state dye-sensitized solar cells with high efficiency. Nature. 2012;485(7399):486-489.

[11] Nozik AJ. Spectroscopy and hot electron relaxation dynamics in semiconductor quantum wells and quantum dots. Annu Rev Phys Chem. 2001;52(1):193-231.

[12] Nozik AJ. Quantum dot solar cells. Phys E. 2002;14(1):115-120.

[13] Kim GH, García de Arquer FP, Yoon YJ, *et al.* High-efficiency colloidal quantum dot photovoltaics via robust self-assembled monolayers. Nano Lett. 2015;15(11):7691-7696.

[14] Griffiths DJ. Introduction to quantum mechanics. Upper Saddle River (NJ): Pearson Education; 2005.

[15] Brus LE. Electron-electron and electron-hole interactions in small semiconductor crystallites: the size dependence of the lowest excited electronic state. J. Chem. Phys. 1984;80(9):4403-4409.

[16] Wang Y, Suna A, Mahler W, *et al.* PbS in polymers - from molecules to bulk solids. J Chem Phys. 1987;87(12):7315-7322.

[17] Kang I, Wise FW. Electronic structure and optical properties of PbS and PbSe quantum dots. J Opt Soc Am B. 1997;14(7):1632-1646.

[18] Hyun BR, Zhong YW, Bartnik AC, *et al.* Electron injection from colloidal PbS quantum dots into titanium dioxide nanoparticles. ACS Nano. 2008;2(11):2206-2212.

[19] Yang Y, Rodriguez-Cordoba W, Xiang X, *et al.* Strong electronic coupling and ultrafast electron transfer between PbS quantum dots and TiO_2 nanocrystalline films. Nano Lett. 2012;12(1):303-309.

[20] Gao J, Johnson JC. Charge trapping in bright and dark states of coupled PbS quantum dot films. ACS Nano. 2012;6(4):3292-3303.

[21] Fernée MJ, Thomsen E, Jensen P, *et al.* Highly efficient luminescence from a hybrid state found in strongly quantum confined PbS nanocrystals. Nanotechnology. 2006;17(4):956.

[22] Lewis J, Wu S, Jiang X. Unconventional gap state of trapped exciton in lead sulfide quantum dots. Nanotechnology. 2010;21(45):455402.

[23] Wanger DD, Correa RE, Dauler EA, *et al.* The dominant role of exciton quenching in PbS quantum-dot-based photovoltaic devices. Nano Lett. 2013;13(12):5907-5912.

[24] Bockelmann U, Bastard G. Phonon scattering and energy relaxation in two-, one-, and zero-dimensional electron gases. Phys Rev B. 1990;42(14):8947.

[25] Benisty H, Sotomayor-Torres C, Weisbuch C. Intrinsic mechanism for the poor luminescence properties of quantum-box systems. Phys Rev B. 1991;44(19):10945.

[26] Pelouch WS, Ellingson RJ, Powers PE, *et al.* Investigation of hot-carrier relaxation in quantum-well and bulk GaAs at high carrier densities. Semicond Sci Technol. 1992;7(3B):B337-B339.

[27] Rosenwaks Y, Hanna MC, Levi DH, *et al.* Hot-carrier cooling in GaAs quantum-wells vs bulk. Phys Rev B. 1993;48(19):14675-14678.

[28] Pelouch WS, Ellingson RJ, Powers PE, *et al.* Comparison of hot-carrier relaxation in quantum-wells and bulk GaAs at high carrier densities. Phys Rev B. 1992;45(3):1450-1453.

[29] Beard MC, Luther JM, Semonin OE, *et al.* Third generation photovoltaics based on multiple exciton generation in quantum confined semiconductors. Acc Chem Res. 2012;46(6):1252-1260.

[30] Semonin OE, Luther JM, Choi S, *et al.* Peak external photocurrent quantum efficiency exceeding 100% via MEG in a quantum dot solar cell. Science. 2011;334(6062):1530-3.

[31] Böhm ML, Jellicoe TC, Tabachnyk M, *et al.* Lead telluride quantum dot solar cells displaying external quantum efficiencies exceeding 120%. Nano Lett. 2015;15(12):7987-93.

[32] Davis NJ, Böhm ML, Tabachnyk M, *et al.* Multiple-exciton generation in lead selenide nanorod solar cells with external quantum efficiencies exceeding 120%. Nat. Comm. 2015;6.

[33] Ellingson RJ, Beard MC, Johnson JC, *et al.* Highly efficient multiple exciton generation in colloidal PbSe and PbS quantum dots. Nano Lett. 2005;5(5):865-871.

[34] Schaller RD, Sykora M, Jeong S, *et al.* High-efficiency carrier multiplication and ultrafast charge separation in semiconductor nanocrystals studied via time-resolved photoluminescence. J Phys Chem B. 2006;110(50):25332-25338.

[35] Schaller RD, Klimov VI. High efficiency carrier multiplication in PbSe nanocrystals: implications for solar energy conversion. Phys Rev Lett. 2004;92(18):186601.

[36] Hanna M, Nozik AJ. Solar conversion efficiency of photovoltaic and photoelectrolysis cells with carrier multiplication absorbers. J Appl Phys. 2006;100(7):074510.

[37] König D, Casalenuovo K, Takeda Y, *et al.* Hot carrier solar cells: principles, materials and design. Phys E. 2010;42(10):2862-2866.

[38] Semonin OE, Luther JM, Choi S, *et al.* Peak external photocurrent quantum efficiency exceeding 100% via MEG in a quantum dot solar cell. Science. 2011;334(6062):1530-1533.

[39] Beard MC, Midgett AG, Law M, *et al.* Variations in the quantum efficiency of multiple exciton generation for a series of chemically treated PbSe nanocrystal films. Nano Lett. 2009;9(2):836-845.

[40] Luther JM, Beard MC, Song Q, *et al.* Multiple exciton generation in films of electronically coupled PbSe quantum dots. Nano Lett. 2007;7(6):1779-1784.

[41] Lee JS, Kovalenko MV, Huang J, *et al.* Band-like transport, high electron mobility and high photoconductivity in all-inorganic nanocrystal arrays. Nat Nanotechnol. 2011;6(6):348-352.

[42] Takeda Y, Motohiro T, König D, *et al.* Practical factors lowering conversion efficiency of hot carrier solar cells. Appl Phys Express, 2010;3(10):104301.

[43] Nozik AJ, Beard MC, Luther JM, *et al.* Semiconductor quantum dots and quantum dot arrays and applications of multiple exciton generation to third-generation photovoltaic solar cells. Chem Rev. 2010;110(11):6873-6890.

[44] Okada Y, Morioka T, Yoshida K, *et al.* Increase in photocurrent by optical transitions via intermediate quantum states in direct-doped InAs/GaNAs strain-compensated quantum dot solar cell. J Appl Phys. 2011;109(2):024301.

[45] Robinson RD, Sadtler B, Demchenko DO, *et al.* Spontaneous superlattice formation in nanorods through partial cation exchange. Science. 2007;317(5836):355-358.

[46] Yu P, Cardona M. Fundamentals of semiconductors: physics and materials properties. [New York (NY)]: Springer Science & Business Media; 2010.

[47] Matthews D, Summers H, Smowton P, *et al.* Experimental investigation of the effect of wetting-layer states on the gain-current characteristic of quantum-dot lasers. Appl Phys Lett. 2002;81(26):4904-4906.

[48] Bailey CG, Forbes DV, Polly SJ, *et al.* Open-circuit voltage improvement of InAs/GaAs quantum-dot solar cells using reduced InAs coverage. IEEE J Photovolt. 2012;2(3):269-275.

[49] Raviswaran A, Liu CP, Kim J, *et al.* Evolution of coherent islands during strained-layer Volmer-Weber growth of Si on Ge (111). Phys Rev B. 2001;63(12):125314.

[50] Benyoucef M, Reithmaier J. Direct growth of III–V quantum dots on silicon substrates: structural and optical properties. Semicond Sci Technol. 2013;28(9):094004.

[51] Schmidt V, Witteman JV, Gösele U. Growth, Thermodynamics, and electrical properties of silicon nanowires. Chem Rev. 2010;110(1):361-388.

[52] Schmidt V, Senz S, Gösele U. UHV chemical vapour deposition of silicon nanowires. Zeitschrift für Metallkunde. 2005;96(5):427-428.

[53] Trentler TJ, Hickman KM, Goel SC, *et al.* Solution-liquid-solid growth of crystalline Ill-V semiconductors: an analogy to vapor-liquid-solid growth. Science. 1995;270(5243):1791-1794.

[54] Westwater J, Gosain D, Tomiya S, *et al.* Growth of silicon nanowires via gold/silane vapor–liquid–solid reaction. J Vac Sci Technol B Nanotechnol Microelectron Mater, Process, Meas, Phenom. 1997;15(3):554-557.

[55] Wu Y, Yang P. Direct observation of vapor-liquid-solid nanowire growth. J Am Chem Soc. 2001;123(13):3165-3166.

[56] Vogel R, Hoyer P, Weller H. Quantum-sized PbS, CdS, Ag_2S, Sb_2S_3 and Bi_2S_3 particles as sensitizers for various nanoporous wide-bandgap semiconductors. J Phys Chem. 1994;98(12):3183-3188.

[57] Kamat PV. Quantum dot solar cells: Semiconductor nanocrystals as light harvesters. J Phys Chem C. 2008;112(48):18737-18753.

[58] Faraday M. The Bakerian lecture: experimental relations of gold (and other metals) to light. Philos Trans R Soc London. 1857;147:145-181.

[59] Peng XG, Wickham J, Alivisatos AP. Kinetics of II-VI and III-V colloidal semiconductor nanocrystal growth: "Focusing" of size distributions. J Am Chem Soc. 1998:120(21):LBNL-41792.

[60] Qu LH, Yu WW, Peng XP. In situ observation of the nucleation and growth of CdSe nanocrystals. Nano Lett. 2004;4(3)465-469.

[61] Xie R, Li Z, Peng X. Nucleation kinetics vs chemical kinetics in the initial formation of semiconductor nanocrystals. J Am Chem Soc. 2009;131(42):15457-15466.

[62] Murray CB, Norris DJ, Bawendi MG. Synthesis and characterization of nearly monodisperse CdE (E = S, Se, Te) semiconductor nanocrystallites. J Am Chem Soc. 1993;115(19):8706-8715.

[63] Murray CB, Kagan C, Bawendi MG. Synthesis and characterization of monodisperse nanocrystals and close-packed nanocrystal assemblies. Ann Rev Mater Sci. 2000;30(1):545-610.

[64] Murray CB, Sun SH, Gaschler W, *et al.* Colloidal synthesis of nanocrystals and nanocrystal superlattices. IBM J Res Dev. 2001;45(1):47-56.

[65] Jin T, Fujii F, Sakata H, *et al.* Amphiphilic p-sulfonatocalix[4]arene-coated CdSe/ZnS quantum dots for the optical detection of the neurotransmitter acetylcholine. Chem Comm. 2005;(34):4300-4302.

[66] Hines MA, Scholes GD. Colloidal PbS nanocrystals with size-tunable near-infrared emission: Observation of post-synthesis self-narrowing of the particle size distribution. Adv Mater. 2003;15(21):1844-1849.

[67] Lim X. The nanolight revolution is coming. Nature. 2016;531(7592):26-28).

[68] Emin S, Singh SP, Han L, *et al.* Colloidal quantum dot solar cells. Sol Energy. 2011;85(6):1264-1282.

[69] Pattantyus-Abraham AG, Kramer IJ, Barkhouse AR, *et al.* Depleted-heterojunction colloidal quantum dot solar cells. ACS Nano. 2010;4(6) :3374-3380.

[70] Huynh WU, Dittmer JJ, Alivisatos AP. Hybrid nanorod-polymer solar cells. Science. 2002;295(5564):2425-2427.

[71] Ren S, Chang LY, Lim SK, *et al.* Inorganic-organic hybrid solar cell: bridging quantum dots to conjugated polymer nanowires. Nano Lett. 2011;11(9):3998-4002.

[72] Liu J, Tanaka T, Sivula K, *et al.* Employing end-functional polythiophene to control the morphology of nanocrystal-polymer composites in hybrid solar cells. J Am Chem Soc. 2004;126(21):6550-6551.

[73] McDonald SA, Konstantatos G, Zhang S, *et al.* Solution-processed PbS quantum dot infrared photodetectors and photovoltaics. Nat Mater. 2005;4(2):138-142.

[74] Ryan JW, Marin-Beloqui JM, Albero J, *et al.* Nongeminate recombination dynamics-device voltage relationship in hybrid PbS quantum dot/C60 solar cells. J Phys Chem C. 2013;117(34):17470-17476.

[75] Zhou Y, Eck M, Veit C, *et al.* Efficiency enhancement for bulk-heterojunction hybrid solar cells based on acid treated CdSe quantum dots and low bandgap polymer PCPDTBT. Sol Energy Mater Sol Cells. 2011;95(4):1232-1237.

[76] Li Y, Hu Y, Zhao Y, *et al.* An electrochemical avenue to green-luminescent graphene quantum dots as potential electron-acceptors for photovoltaics. Adv. Mater. 2011;23(6):776-780.

[77] Guo CX, Yang HB, Sheng ZM, *et al.* Layered graphene/quantum dots for photovoltaic devices. Angew Chem, Int Ed. 2010;49(17):3014-3017.

[78] Landi B, Castro S, Ruf H, *et al.* CdSe quantum dot-single wall carbon nanotube complexes for polymeric solar cells. Sol Energy Mater Sol Cells. 2005;87(1):733-746.

[79] Lee YL, Chang CH. Efficient polysulfide electrolyte for CdS quantum dot-sensitized solar cells. J Power Sources. 2008;185(1):584-588.

[80] Lee HJ, Chen P, Moon SJ, *et al.* Regenerative PbS and CdS quantum dot sensitized solar cells with a cobalt complex as hole mediator. Langmuir. 2009;25(13):7602-7608.

[81] Lee H, Leventis HC, Moon SJ, *et al.* PbS and CdS quantum dot-sensitized solid-state solar cells:"Old concepts, new results". Adv Funct Mater. 200;19(17):2735-2742.

[82] Mora-Seró I, Gimenez S, Fabregat-Santiago F, *et al.* Recombination in quantum dot sensitized solar cells. Acc Chem Res. 2009;42(11):1848-1857.

[83] Tenne R, Hodes G. Improved efficiency of CdSe photoanodes by photoelectrochemical etching. Appl Phys Lett. 2008;37(4):428-430.

[84] Shen Q, Kobayashi J, Diguna LJ, *et al.* Effect of ZnS coating on the photovoltaic properties of CdSe quantum dot-sensitized solar cells. J Appl Phys. 2008;103(8):084304.

[85] Radich JG, Dwyer R, Kamat PV. Cu_2S reduced graphene oxide composite for high-efficiency quantum dot solar cells. Overcoming the redox limitations of S^{2-} /Sn^{2-} at the counter electrode. J Phys Chem Lett. 2011;2(19):2453-2460.

[86] Lee YL, Huang BM, Chien HT. Highly efficient CdSe-sensitized TiO2 photoelectrode for quantum-dot-sensitized solar cell applications. Chem Mater. 2008;20(22):6903-6905.

[87] González-Pedro V, Xu X, Mora-Sero I, *et al.* Modeling high-efficiency quantum dot sensitized solar cells. ACS Nano. 2010;4(10):5783-5790.

[88] Diguna LJ, Shen Q, Kobayashi J, *et al.* High efficiency of CdSe quantum-dot-sensitized TiO_2 inverse opal solar cells. Appl Phys Lett. 2007;91(2):023116-023113.

[89] Rühle S, Shalom M, Zaban A. Quantum-dot-sensitized solar cells. ChemPhysChem. 2010;11(11):2290-2304.

[90] Zhao K, Pan Z, Mora-Seró I, *et al.* Boosting power conversion efficiencies of quantum-dot-sensitized solar cells beyond 8% by recombination control. J Am Chem Soc. 2015;137(6):5602-5609.

[91] Luther JM, Law M, Beard MC, *et al.* Schottky solar cells based on colloidal nanocrystal films. Nano Lett. 2008;8(10):3488-3492.

[92] Strasfeld DB, Dorn A, Wanger DD, *et al.* Imaging Schottky barriers and ohmic contacts in PbS quantum dot devices. Nano Lett. 2012;12(2):569-575.

[93] Piliego C, Protesescu L, Bisri SZ, *et al.* 5.2% efficient PbS nanocrystal Schottky solar cells. Energy Environ Sci. 2013;6(10):3054-3059.

[94] Liu H, Zhitomirsky D, Hoogland S, *et al.* Systematic optimization of quantum junction colloidal quantum dot solar cells. Appl Phys Lett. 2012;101(15):151112.

[95] Liu H, Tang J, Kramer IJ, *et al.* Electron acceptor materials engineering in colloidal quantum dot solar cells. Adv Mater. 2011;23(33):3832-3837.

[96] Tang J, Kemp KW, Hoogland S, *et al.* Colloidal-quantum-dot photovoltaics using atomic-ligand passivation. Nat Mater. 2011;10(10):765-771.

[97] Ip AH, Thon SM, Hoogland S, *et al.* Hybrid passivated colloidal quantum dot solids. Nat Nanotechnol. 2012;7(9):577-582.

[98] Ning Z, Zhitomirsky D, Adinolfi V, *et al.* Graded doping for enhanced colloidal quantum dot photovoltaics. Adv Mater. 2013;25(12):1719-1723.

[99] Tang J, Liu H, Zhitomirsky D, *et al.* Quantum junction solar cells. Nano Lett. 2012;12(9) :4889-4894.

[100] Kramer IJ, Levina L, Debnath R, *et al.* Solar cells using quantum funnels. Nano Lett. 2011;11(9):3701-3706.

[101] Wang X, Koleilat GI, Tang J, *et al.* Tandem colloidal quantum dot solar cells employing a graded recombination layer. Nat Photonics. 2011;5(8):480-484.

[102] Cotton FA, Wilkinson G, Murillo CA, *et al.* Advanced Inorganic Chemistry, 6th edition. [New Delhi (India)]: Wiley India Pvt Limited; 2007.

[103] Mazumder S, Dey R, Mitra M, *et al.* Review: biofunctionalized quantum dots in biology and medicine. J Nanomater. 2009;2009:38.

[104] Algar WR, Tavares AJ, Krull UJ. Beyond labels: a review of the application of quantum dots as integrated components of assays, bioprobes, and biosensors utilizing optical transduction. Anal Chim Acta. 2010;673(1):1-25.

[105] Konstantatos G, Sargent EH. Colloidal quantum dot optoelectronics and photovoltaics. Cambridge (United Kingdom): Cambridge University Press; 2013.

[106] Moody IS, Stonas AR, Lonergan MC. PbS nanocrystals functionalized with a short-chain, ionic, dithiol ligand. J Phys Chem C. 2008;112(49):19383-19389.

[107] Luther JM, Law M, Song Q, *et al.* Structural, optical and electrical properties of self-assembled films of PbSe nanocrystals treated with 1,2-ethanedithiol. ACS Nano. 2008;2(2):271-280.

[108] Barkhouse DAR, Pattantyus-Abraham AG, Levina L. *et al.* Thiols passivate recombination centers in colloidal quantum dots leading to enhanced photovoltaic device efficiency. ACS Nano. 2008;2(11):2356-2362.

[109] Szendrei K, Gomulya W, Yarema M, *et al.* PbS nanocrystal solar cells with high efficiency and fill factor. Appl Phys Lett. 2010;97(20):203501.

[110] Xu F, Benavides J, Ma X, *et al.* Interconnected TiO2 nanowire networks for PbS quantum dot solar cell applications. J Nanotechnol. 2012;2012:709031.

[111] Padilla D, Zhai G, Breeze AJ, *et al.* Thermal properties of TiO_2/PbS nanoparticle solar cells. Nanomater Nanotechnol. 2012;2:18.

[112] Klem EJ, Shukla H, Hinds S, *et al.* Impact of dithiol treatment and air annealing on the conductivity, mobility, and hole density in PbS colloidal quantum dot solids. Appl Phys Lett. 2008;92(21):212105.

[113] Inerbaev TM, Masunov AE, Khondaker SI, *et al.* Quantum chemistry of quantum dots: Effects of ligands and oxidation. J Chem Phys. 2009;131(4):044106.

[114] Voznyy O, Zhitomirsky D, Stadler P, *et al.* A charge-orbital balance picture of doping in colloidal quantum dot solids. ACS Nano. 2012;6(9):8448-8455.

[115] Jeong KS, Tang J, Liu H, *et al.* Enhanced mobility-lifetime products in PbS colloidal quantum dot photovoltaics. ACS Nano. 2012;6(1):89-99.

[116] Zherebetskyy D, Scheele M, Zhang Y, *et al.* Hydroxylation of the surface of PbS nanocrystals passivated with oleic acid. Science. 2014;344(6190):1380-1384.

[117] Malgras V, Nattestad A, Yamauchi Y, *et al.* The effect of surface passivation on the structure of sulphur-rich PbS colloidal quantum dots for photovoltaic application. Nanoscale. 2015;7(13):5706-5711.

[118] Tang J, Brzozowski L, Barkhouse DAR, *et al.* Quantum dot photovoltaics in the extreme quantum confinement regime: The surface-chemical origins of exceptional air- and light-stability. ACS Nano. 2010;4(2):869-878.

[119] Koleilat GI, Levina L, Shukla H, *et al.* Efficient, stable infrared photovoltaics based on solution-cast colloidal quantum dots. ACS Nano. 2008;2(5):833-840.

[120] Giansante C, Infante I, Fabiano E, *et al.* "Darker-than-Black" PbS Quantum Dots: Enhancing Optical Absorption of Colloidal Semiconductor Nanocrystals via Short Conjugated Ligands. J Am Chem Soc. 2015;137(5):1875-86.

[121] Kovalenko MV, Bodnarchuk MI, Zaumseil J, *et al.* Expanding the chemical versatility of colloidal nanocrystals capped with molecular metal chalcogenide ligands. J Am Chem Soc. 2010;132(29):10085-10092.

[122] Kovalenko MV, Scheele M, Talapin DV. Colloidal nanocrystals with molecular metal chalcogenide surface ligands. Science. 2009;324(5933):1417-1420.

[123] Nag A, Kovalenko MV, Lee JS, *et al.* Metal-free inorganic ligands for colloidal nanocrystals: S^{2-}, HS^{-}, Se^{2-}, HSe^{-}, Te^{2-}, HTe^{-}, TeS_3^{2-}, OH^{-}, and NH_2^{-} as surface ligands. J Am Chem Soc. 2011;133(27):10612-10620.

[124] Yang Y, Zheng Y, Cao W, *et al.* High-efficiency light-emitting devices based on quantum dots with tailored nanostructures. Nat Photonics. 2015.

[125] Supran GJ, Song KW, Hwang GW, *et al.* High-performance shortwave-infrared light-emitting devices using core-shell (PbS-CdS) colloidal quantum dots. Adv Mater. 2015;27(8):1437-42.

[126] Bae WK, Joo J, Padilha LA, *et al.* Highly effective surface passivation of PbSe quantum dots through reaction with molecular chlorine. J Am Chem Soc. 2012;134(49):20160-20168.

[127] Zanella M, Maserati L, Pernia Leal M, *et al.* Atomic ligand passivation of colloidal nanocrystal films via their reaction with propyltrichlorosilane. Chem Mater. 2013;25(8):1423-1429.

[128] Zhang H, Hu B, Sun L, *et al.* Surfactant ligand removal and rational fabrication of inorganically connected quantum dots. Nano Lett. 2011;11(12):5356-5361.

[129] Cate St, Liu Y, Schins JM, *et al.* Phonons do not assist carrier multiplication in PbSe quantum dot solids. J Phys Chem Lett. 2013;4(19):3257-3262.

[130] Kinder E, Moroz P, Diederich G, *et al.* Fabrication of all-inorganic nanocrystals solids through matrix encapsulation of nanocrystal arrays. J Am Chem Soc. 2011;133(50):20488-20499.

[131] Ning Z, Ren Y, Hoogland S, *et al.* All-inorganic colloidal quantum dot photovoltaics employing solution-phase halide passivation. Adv Mater. 2012;24(47):6295-6299.

[132] Zhitomirsky D, Furukawa M, Tang J, *et al.* N-type colloidal-quantum-dot solids for photovoltaics. Adv Mater. 2012;24(46):6181-6185.

[133] Thon SM, Ip AH, Voznyy O, *et al.* Role of bond adaptability in the passivation of colloidal quantum dot solids. ACS Nano. 2013;7(9):7680-7688.

[134] Mora-Sero I, Bertoluzzi L, Gonzalez-Pedro V, *et al.* Selective contacts drive charge extraction in quantum dot solids via asymmetry in carrier transfer kinetics. Nat Commun. 2013;4:2272.

[135] Malgras V, Zhang G, Nattestad A, *et al.* Trap-assisted transport and non-uniform charge distribution in sulfur-rich PbS colloidal quantum dot-based solar cells with selective contacts. ACS applied materials & interfaces. 2015;7(48):26455-26460.

[136] Yuan M, Voznyy O, Zhitomirsky D, *et al.* Synergistic doping of fullerene electron transport layer and colloidal quantum dot solids enhances solar cell performance. Adv. Mater. 2015;27(5):917-921.

[137] Maraghechi P, Labelle AJ, Kirmani AR, *et al.* The donor–supply electrode enhances performance in colloidal quantum dot solar cells. ACS Nano. 2013;7(7):6111-6116.

[138] Ehrler B, Musselman KP, Böhm ML, *et al.* Preventing interfacial recombination in colloidal quantum dot solar cells by doping the metal oxide. ACS Nano. 2013;7(5):4210-4220.

[139] Willis SM, Cheng C, Assender HE, *et al.* The transitional heterojunction behavior of PbS/ZnO colloidal quantum dot solar cells. Nano Lett. 2012;12(3):1522-1526.

[140] Wang X, Koleilat GI, Fischer A, *et al.* Enhanced open-circuit voltage in visible quantum dot photovoltaics by engineering of carrier-collecting electrodes. ACS Appl Mater Interfaces. 2011;3(10):3792-3795.

[141] Jean J, Chang S, Brown PR, *et al.* ZnO nanowire arrays for enhanced photocurrent in PbS quantum dot solar cells. Adv Mater. 2013;25(20):2790-2796.

[142] Debnath R, Tang J, Barkhouse DA, *et al.* Ambient-processed colloidal quantum dot solar cells via individual pre-encapsulation of nanoparticles. J Am Chem Soc. 2010;132(17):5952-5953.

[143] Tang J, Wang X, Brzozowski L, *et al.* Schottky quantum dot solar cells stable in air under solar illumination. Adv Mater. 2010;22(12):1398-1402.

[144] Johnston KW, Pattantyus-Abraham AG, Clifford JP, *et al.* Schottky-quantum dot photovoltaics for efficient infrared power conversion. Appl Phys Lett. 2008;92(15):151115.

[145] Etgar L, Moehl T, Gabriel S, *et al.* Light energy conversion by mesoscopic PbS quantum dots/TiO_2 heterojunction solar cells. ACS Nano. 2012;6(4):3092-3099.

[146] Brown PR, Lunt RR, Zhao N, *et al.* Improved current extraction from ZnO/PbS quantum dot heterojunction photovoltaics using a MoO3 interfacial layer. Nano Lett. 2011;11(7):2955-2961.

[147] Gao J, Perkins CL, Luther JM, *et al.* n-type transition metal oxide as a hole extraction layer in PbS quantum dot solar cells. Nano Lett. 2011;11(8):3263-3266.

[148] Gao JB, Luther JM, Semonin OE, *et al.* Quantum dot size dependent J-V characteristics in heterojunction ZnO/PbS quantum dot solar cells. Nano Lett. 2011;11(3):1002-1008.

[149] Bakulin AA, Neutzner S, Bakker HJ, *et al.* Charge trapping dynamics in PbS colloidal quantum dot photovoltaic devices. ACS Nano. 2013;7(10):8771-8779.

[150] Zhitomirsky D, Voznyy O, Hoogland S, *et al.* Measuring charge carrier diffusion in coupled colloidal quantum dot solids. ACS Nano. 2013;7(6):5282-5290.

[151] Whitham K, Yang J, Savitzky BH, *et al.* Charge transport and localization in atomically coherent quantum dot solids. Nat Mater. 2016;15(5):557-63.

[152] Guyot-Sionnest P, Wehrenberg B, Yu D. Intraband relaxation in CdSe nanocrystals and the strong influence of the surface ligands. J Chem Phys. 2005;123(7):074709.

[153] Nagpal P, Klimov VI. Role of mid-gap states in charge transport and photoconductivity in semiconductor nanocrystal films. Nat Comm. 2011;2:486.

[154] Stadler P, Sutherland BR, Ren Y, *et al.* Joint mapping mobility and trap density in colloidal quantum dots solids. ACS Nano. 2013;7(7):5757-5762.

[155] Lan X, Voznyy O, Kiani A, *et al.* Passivation using molecular halides increases quantum dot solar cell performance. Adv Mater. 2016;28(2):299-304.

[156] Yang Z, Janmohamed A, Lan X, *et al.* Colloidal quantum dot photovoltaics enhanced by perovskite shelling. Nano Lett. 2015;15(11):7539-7543.

[157] Lan X, Voznyy O, García del Arquer FP, *et al.* 10.6% certified colloidal quantum dot solar cells via solvent-polarity-engineered halide passivation. Nano Lett. 2016;16(7):4630-4634.

[158] Zhang X, Hägglund C, Johansson EM. Highly efficient, transparent and stable semitransparent colloidal quantum dot solar cells: a combined numerical

modeling and experimental approach. Energy Environ Sci. 2017 [cited on 2017 Jan 11]; [9 pages]. DOI:10.1039/C6EE02824A

[159] Cappelluti F, Gioannini M, Khalili A. Impact of doping on InAs/GaAs quantum-dot solar cells: A numerical study on photovoltaic and photoluminescence behavior. Sol Energy Mater Sol Cells. 2016;31(157):209-220.

[160] So D, Pradhan S, Konstantatos G. Solid-state colloidal CuInS 2 quantum dot solar cells enabled by bulk heterojunctions. Nanoscale. 2016;8(37):16776-16785.

[161] Gonzalez-Carrero S, Francés-Soriano L, González-Béjar M, *et al.* The luminescence of CH3NH3PbBr3 perovskite nanoparticles crests the summit and their photostability under wet conditions is enhanced. Small. 2016;12(38):5245-5250.

[162] Swarnkar A, Marshall AR, Sanehira EM, *et al.* Quantum dot-induced phase stabilization of α-CsPbI3 perovskite for high-efficiency photovoltaics. Science. 2016;354(6308):92-95.

[163] Malgras V, Tominaka S, Ryan JW, *et al.* Observation of quantum confinement in monodisperse methylammonium lead halide perovskite nanocrystals embedded in mesoporous silica. J Am Chem Soc. 2016;138(42):13874-13881.

[164] Malgras V, Henzie J, Takei T, *et al.* Hybrid methylammonium lead halide perovskite nanocrystals confined in gyroidal silica templates. Chem Comm. 2017;53:2359-2362.

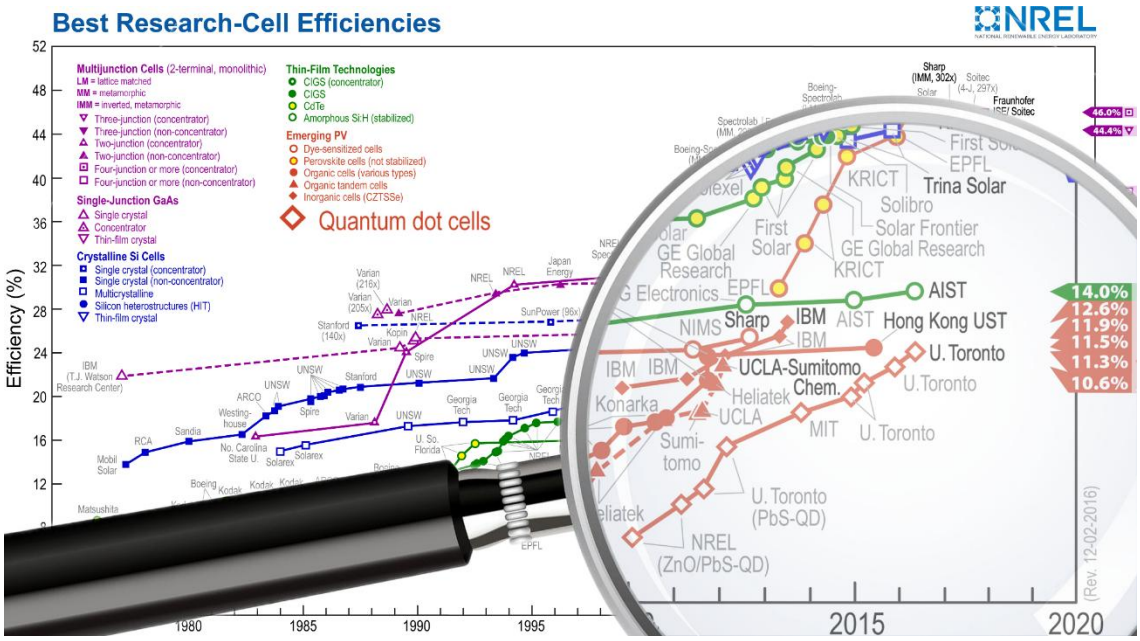

Figure 1. NREL efficiency chart, emphasizing on the recent development in quantum dot solar cells. Adapted from the NREL efficiency chart [6]

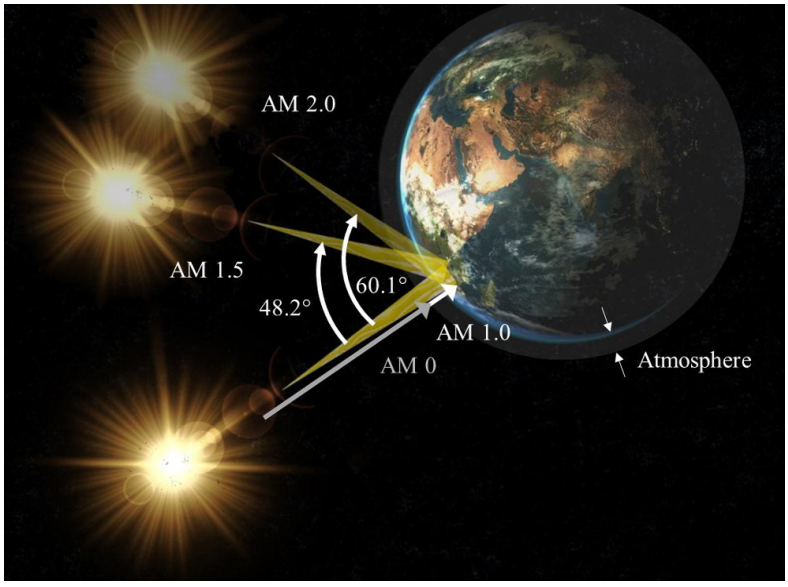

Figure 2. Geometric representations of the various solar spectrum standards AM 0, AM 1.0, AM1.5 and AM 2.0.

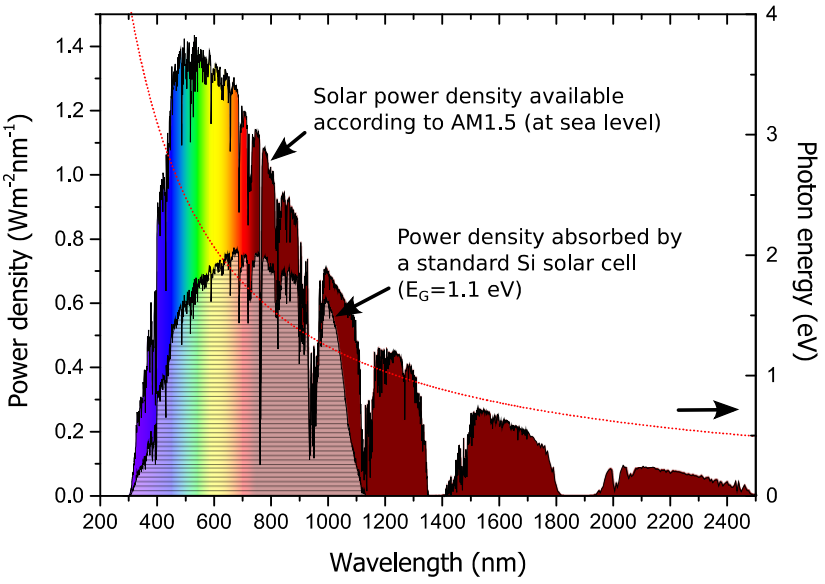

Figure 3. AM 1.5 (blue) solar power and proportion which is actually absorbed by a standard crystalline silicon solar cell (purple). The orange dashed line represents the energy carried per photon at a specific wavelength.

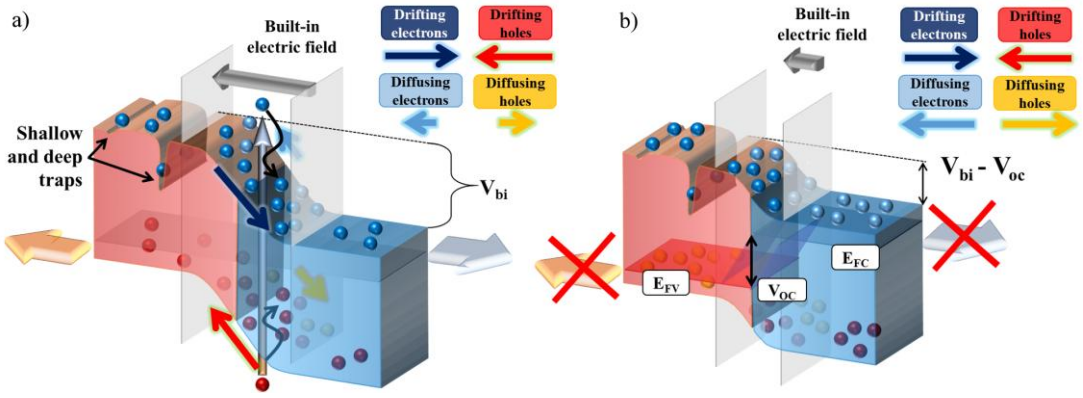

Figure 4. Illustration of the band diagrams at a p-n junction under short-circuit (a) and open-circuit (b) conditions. Vbi, EFV and E

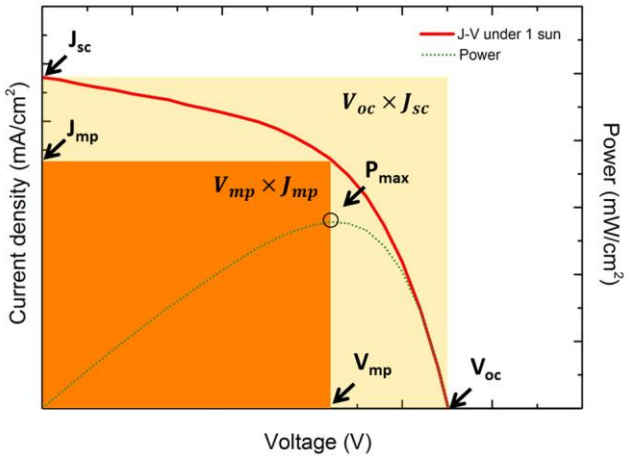

Figure 5. a) Typical J-V curve and main parameters as defined in the text.

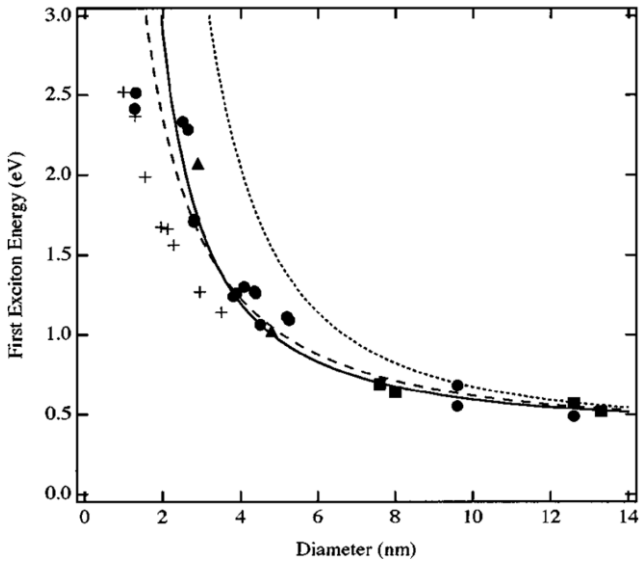

Figure 6. First excitonic energy dependence on the crystal diameter of the effective mass model (dotted curve), the hyperbolic model (dashed curve), and the 4-band model (solid curve). Symbols are experimental data from various publications. Reprinted with permission from [17]. Copyright 1997 Optical Society of America.

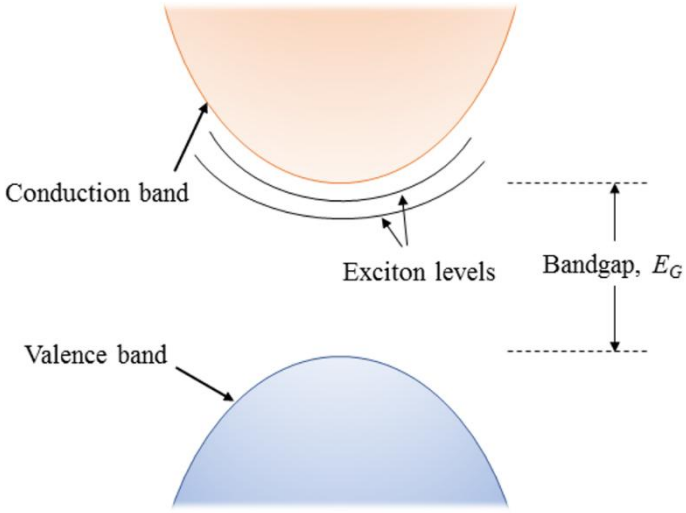

Figure 7. Schematic representation of excitonic levels located within the bandgap.

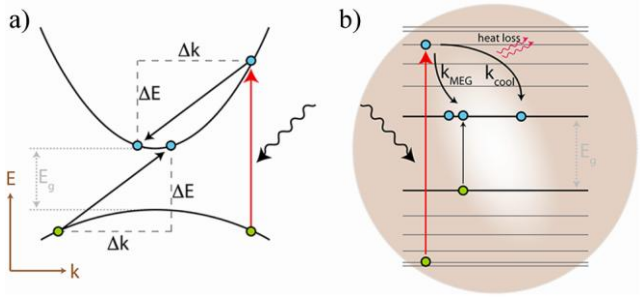

Figure 8. Fast relaxation in continuous energy levels ($\boldsymbol{\delta E}$) and conservation of crystal momentum ($\boldsymbol{\Delta k}$) in (a) bulk semiconductors versus (b) MEG in nanocrystals. Reprinted with permission from [29]. Copyright 2013 American Chemical Society.

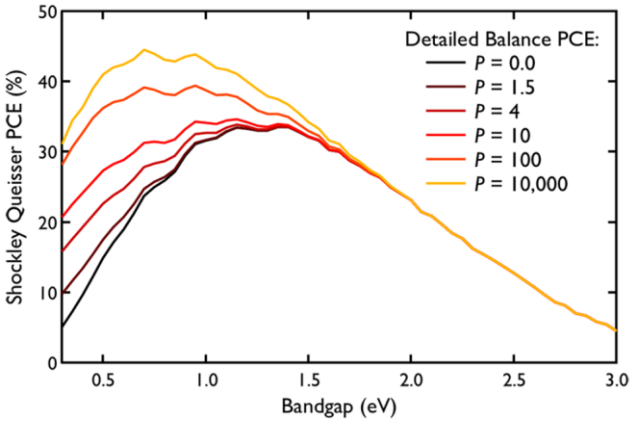

Figure 9. Theoretical improvement of the Shockley-Queisser limit due to the MEG efficiency P. PCE: Photoconversion efficiency. Reprinted with permission from [29]. Copyright 2013 American Chemical Society.

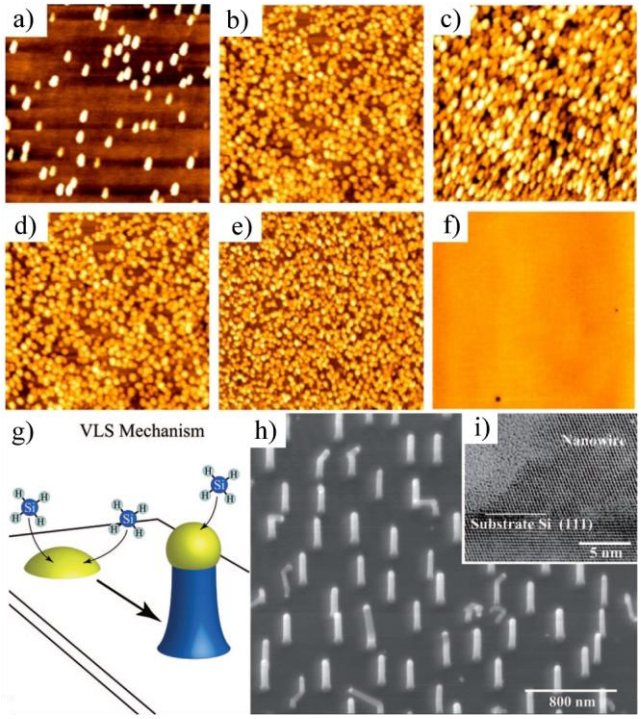

Figure 10. InAs islands grown at different V/III ratios [a) 15, b) 25, c) 35] and different temperatures [d) 400 °C, e) 450 °C, f) 500 °C]. Reprinted with permission from [50]. Copyright 2013 Institute of Physics. (g) Schematic of VLS mechanism. Reprinted with permission from [51]. Copyright 2010 American Chemical Society. Low (h) and high resolution (i) transmission electron microscopy images of Si nanowires. Reprinted with permission from [52]. Copyright 2005 Hanser.

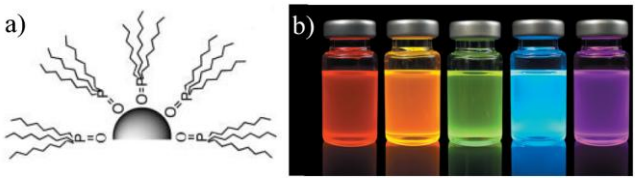

Figure 11. a) QDs capped with tri-n-octylphosphine oxide. Reprinted with permission from [65]. Copyright 2005 Royal Society of Chemistry. b) ZnCdSeS quantum dots with various sizes emitting at various wavelength. Reprinted with permission from [67]. Copyright 2016 Nature Publishing Group.

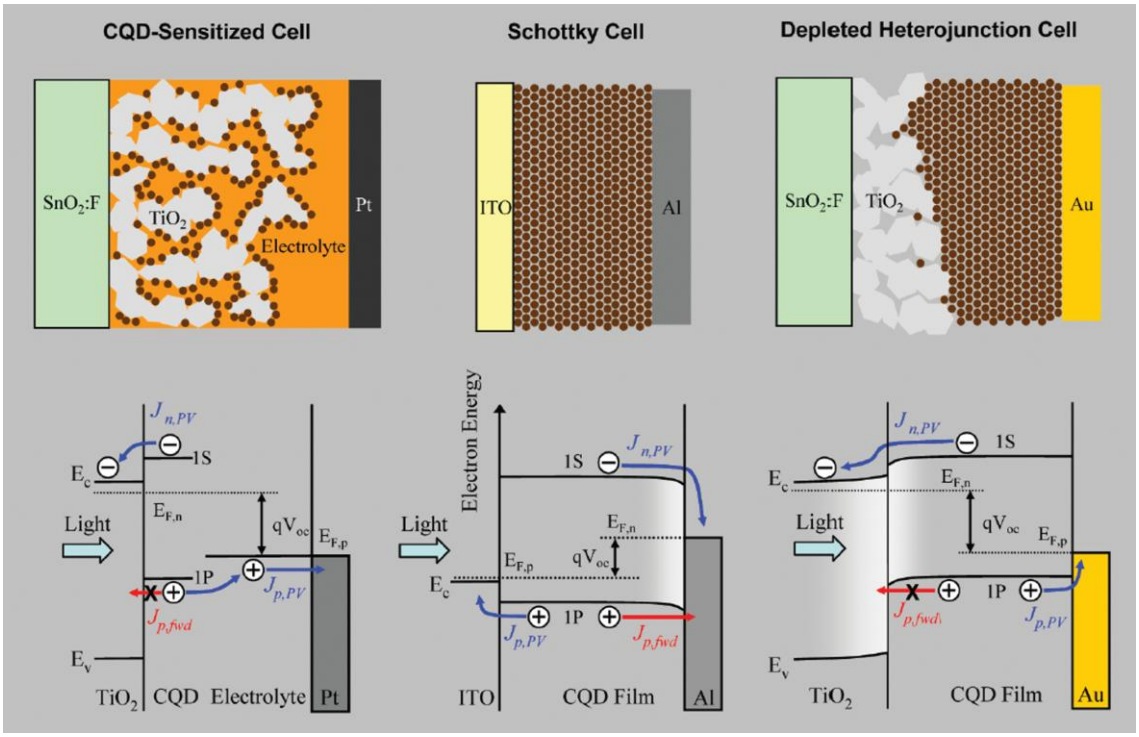

Figure 12. Schematic description of three quantum dot-based solar cells along with band diagrams illustrating the charge dynamic within the device. Reprinted with permission from [69]. ITO stands for indium tin oxide. Copyright 2011 American Chemical Society.

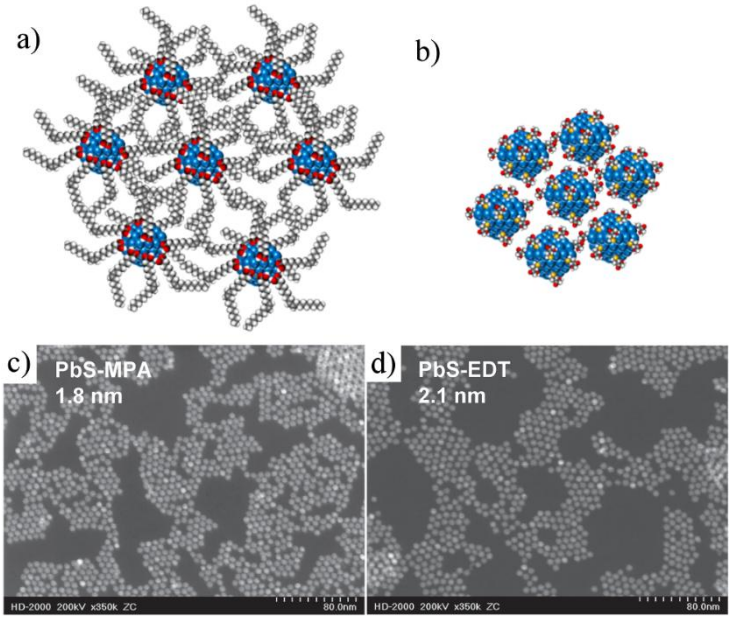

Figure 13. Representation of steric spacing between CQDs when using (a) oleic acid or (b) 3-mercaptopropionic acid. Colour codes are as follows: oxygen: red, carbon: grey, hydrogen: white and sulfur: yellow. Scanning transmission electron microscopy images of CQDs after MPA (c) and EDT (d) ligand exchange. Reprinted with permission from [115]. Copyright 2012 American Chemical Society.

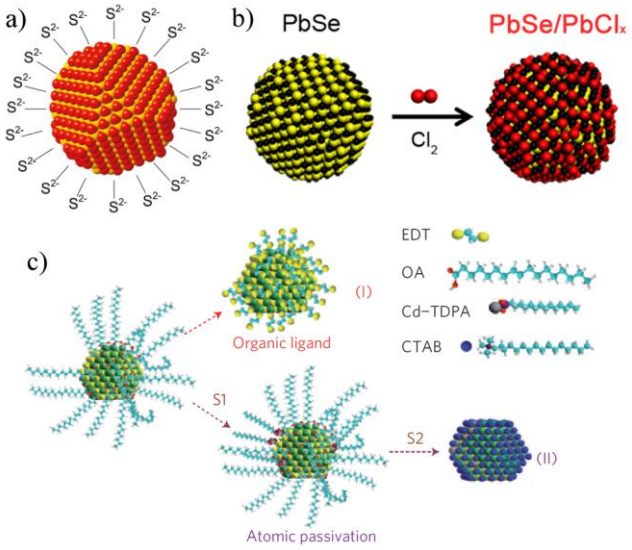

Figure 14. a) S^{2-} inorganic capping. Reprinted with permission from [123]. Copyright 2011 American Chemical Society. b) Atomic-chlorine passivation. Reprinted with permission from [126]. Copyright 2012 American Chemical Society. c) Atomic-ligand

passivation developed by Tang *et al.* OA stands for oleic acid, TDPA for tetradecylphosphonic acid and CTAB for cetyltrimethylammonium bromide. Reprinted with permission from [96]. Copyright 2011 Nature Publishing Group.

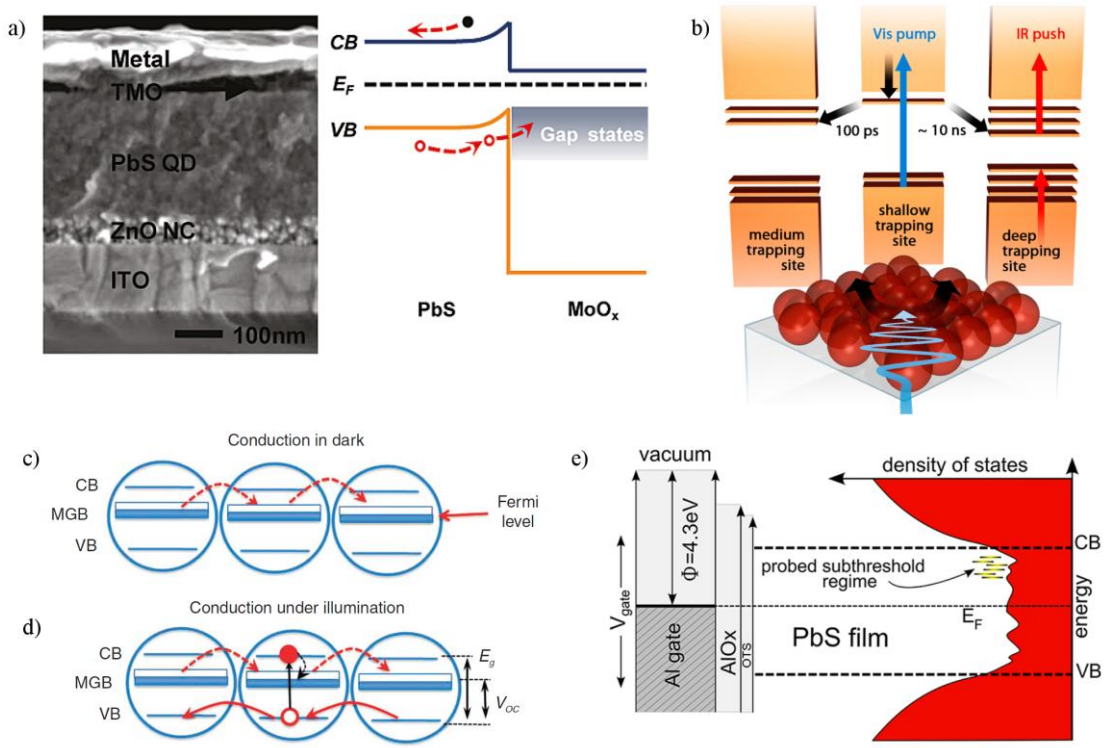

Figure 15. a) Cross-sectional scanning electron microscopy image and band structure of a device with MoO_X selective contact. TMO stands for transition metal oxide, NC for nanocrystal, ITO for indium tin oxide, CB for conduction band and VB for valence band. Reprinted with permission from [147]. Copyright 2011 American Chemical Society. b) Push pump photocurrent method to probe trap states. Reprinted with permission from [149]. Copyright 2013 American Chemical Society. Mid-gap band (MGB) conduction (c) in the dark and (d) under illumination along with simulated density of states. Reprinted with permission from [153]. Copyright 2011 Nature Publishing Group. e) Band diagram showing a schematic density of states in the quantum dot film on the right. Reprinted with permission from [154]. Copyright 2013 American Chemical Society.

	PbS	PbSe	PbTe
ε_∞	17	23	33
E_G (eV)	0.37	0.27	0.32
m_e/m_0	0.080	0.040	0.024
m_h/m_0	0.075	0.034	0.022

Table 1. Dielectric constants (ε_∞), bandgaps (E_G) and reduced masses for electron (m_e/m_0) and holes (m_h/m_0) of lead chalcogenides PbS, PbSe and PbTe.